Investigation of the Geochemical Preservation of ca. 3.0 Ga Permineralized and Encapsulated Microfossils by Nanoscale Secondary Ion Mass Spectrometry

Frédéric Delarue, François Robert, Kenichiro Sugitani, Romain Tartèse, Rémi Duhamel, Sylvie Derenne

Investigation of the geochemical preservation of ca. 3.0 Gyr-old permineralized and encapsulated microfossils by Nanoscale secondary ion mass spectrometry.

Running head: Preservation of encapsulated Archean microfossils.

Frédéric Delarue[1*], François Robert[1], Kenichiro Sugitani[2,3], Romain Tartèse[1], Rémi Duhamel[1], Sylvie Derenne[4]

[1]*IMPMC Sorbonne Universités - MNHN, UPMC Univ Paris 06, UMR CNRS 7590, IRD UMR 206, 61 rue Buffon, F-75005 Paris, France, f.delarue@mnhn.fr, robert@mnhn.fr; romain.tartese@mnhn.fr*

[2]*Department of Environmental Engineering and Architecture, Graduate School of Environmental Studies, Nagoya University, Nagoya, Japan, sugi@info.human.nagoya-u.ac.jp*

[3]*Australian Centre for Astrobiology, University of New South Wales, Sydney, NSW, Australia*

[5]*Sorbonne Universités, UPMC Univ Paris 06, CNRS, UMR 7619 METIS, 4 place Jussieu, F-75005 Paris, France, sylvie.derenne@upmc.fr*

Keywords: Carbonaceous matter - Farrel Quartzite - Fossilization - NanoSIMS ï Nitrogen - Permineralization

* *corresponding author: fdelarue@mnhn.fr*

Abstract

Observations of Archean organic-walled microfossils suggest that their fossilization took place through both encapsulation by silica and permineralization. In this study, we have investigated microfossils from the ca. 3.0 Gyr-old Farrel Quarzite (Pilbara, Western Australia) using transmitted light microscopy, scanning electron microscopy, Raman microspectrometry and NanoSIMS ion microprobe analyses. In contrast to previous statement, we demonstrated that permineralized microfossils were not characterized by the micrometric spatial relationships between Si and C-N as observed in thin sections. Permineralized microfossils are composed of carbonaceous globules that did not survive the acid treatment whereas, encapsulated microfossils were characterized thanks to their resistance to the acid maceration procedure. We have also investigated the microscale relationship between the $^{12}C^{14}N^-$ and $^{12}C_2^-$ ion emission as a proxy of the N/C atomic ratio in both permineralized and encapsulated microfossils. After considering any potential matrix and microtopography effects, we demonstrate that the encapsulated microfossils exhibit the highest level of geochemical preservation. This finding shows that the chemical heterogeneity of the microfossils, observed at a spatial resolution of few hundreds of micrometers, can be related to fossilization processes.

1. Introduction

42 Microfossil-like structures have been reported in numerous Archean rocks (e.g., Walsh, 1992;
43 Schopf, 1993; Javaux et al., 2010; Sugitani et al., 2010). As a result of thermal alteration,
44 however, their morphological features and their geochemical composition had been often
45 severely modified, making the univocal identification of microorganisms and associated
46 metabolism difficult. Microorganisms are generally thought to be fossilized through
47 permineralization resulting from the ñearly infiltration and permeation of tissues by mineral-
48 charged waterò (Schopf 1975). Consequently, the organic remnants are progressively replaced by
49 silica or carbonates during mineralization. However, the presence of organic-walled microfossils
50 in some Archean rocks (Grey and Sugitani, 2009; Javaux et al. 2010; Sugitani et al., 2015) points
51 to the existence of other mechanisms of fossilization, such as encapsulation of microorganisms
52 through nucleation of adjacent mineral crystals for example (Rainey and Jones, 2010). Through
53 investigation of mineralization of microbial mats from Icelandic hot springs, Konhauser and
54 Ferris (1996) proposed that encapsulation favors morphological and geochemical preservation of
55 microorganisms. This is supported by experimental silicification of modern microorganisms,
56 which shows that the negative effect on geochemical preservation caused by thermal alteration
57 can be counter-balanced by encapsulation (Picard et al., 2015). However, encapsulation has not
58 yet been directly documented in Archean rocks despite its great potential for preservation of
59 microorganisms.

60 Bulk N/C atomic ratio has been classically used as a proxy to characterize the
61 preservation status of organic matter (Watanabe et al., 1997; Beaumont and Robert, 1999).
62 However, this bulk geochemical approach neglects potential heterogeneities in preservation
63 among different organic remnants. Recent technological developments, notably in the field of
64 Secondary Ion Mass Spectrometry (SIMS), have allowed *in situ* elemental and isotopic

investigations of putative microfossils at the micro- to nanoscale (Rasmussen et al., 2008; Oehler et al., 2009; House et al., 2013). Notably, it has been shown that the $^{12}C^{14}N^{-}/^{12}C_2^{-}$ molecular ionic ratio is strongly correlated with bulk N/C atomic ratio (Thomen et al., 2014; Alleon et al., 2015), opening up the possibility to evaluate the geochemical preservation of Archean microfossils at the micrometer scale. In pioneering studies, Oehler et al. (2009; 2010) used NanoSIMS analyses to calculate *in situ* N/C atomic ratios ranging from *ca*. 0.0125 to 0.05 for Archean spheroid microfossils from 3.0 Gyr-old cherts. However, the possible effects of microtopography on the $^{12}C^{14}N^{-}/^{12}C_2^{-}$ molecular ratios determined for the microfossils studied by Oehler et al. (2009; 2010) have not been thoroughly evaluated, and it is known that microtopography may induce relatively large changes in $^{12}C^{14}N^{-}/^{12}C_2^{-}$ ratios even though precise quantifications are still incomplete (e.g., Thomen et al., 2014; Alleon et al., 2015). These potential analytical pitfalls have to be addressed to further evaluate the significance of the relatively high *in situ* N/C atomic values determined by Oehler et al. (2009; 2010) for Archean microfossils. In this respect, a recent study has highlighted that silicification promoted the exceptional geochemical preservation of organic microfossils in the 1.88 Gyr-old Gunflint cherts that have N/C atomic ratios up to *ca*. 0.25-0.30 (Alleon et al., 2016), which is commensurable with the N/C ratios of modern cyanobacteria and is, by far, higher than the N/C ratios determined by Oehler et al. (2009, 2010).

In this study, our purposes are (i) to provide a procedure to determine the preservation status of organic microfossils by studying the relationship between the emissions of the $^{12}C_2^{-}$ and $^{12}C^{14}N^{-}$ molecular ions in pure organic standards, kerogens and microfossils from both thin sections and acid maceration residues and (ii) to we discuss the effect of the process of fossilization, i.e. permineralization vs. encapsulation, on the geochemical preservation of microfossils from the 3.0 Gyr-old Farrel Quartzite.

2. Material and Methods

2.1. Sample locality

A black chert sample was collected from the *ca*. 3.0 Ga Farrel Quartzite at the Mount Grant locality in the Goldsworthy greenstone belt, in the Pilbara Craton in Western Australia. The Farrel Quartzite is composed of a clastic formation up to 80 m thick containing fine- to very coarse-grained sandstone, including quartzite with minor conglomerate, mafic to ultra-mafic volcanoclastic layers, evaporite beds and black chert layers (Sugitani et al., 2007). This unit underwent greenschist facies metamorphism and was pervasively silicified. The *ca*. 30 cm thick microfossil-bearing black chert occurs in the uppermost part of the Farrel Quartzite and is closely associated with evaporite beds.

2.2. Analyses

2.2.1. Sample preparations and microscopy

Transmission light microscopy (TLM) observations and NanoSIMS analyses were carried out on both rock thick sections (thickness of *ca*. 50 εm) and isolated kerogen, whereas Scanning Electron Microscope (SEM) observations were only performed on the kerogen. Kerogen isolation was performed on about 200 g of rock through successive demineralization using HF-HCl (Derenne et al., 2008). Then, a few mg of kerogen were deposited on a microscope glass slide for TLM, SEM and NanoSIMS investigations. Carbonaceous microfossils were first observed using TLM in order to define targets of interest. Then, glass slides were directly gold coated (20 nm

thick) for SEM Energy Dispersive X-ray Spectroscopy (EDS) analysis and imaging using a TESCAN VEGA II at the French National Museum of Natural History (MNHN) with an accelerating voltage of 15 kV.

2.2.2. Raman microspectrometry

Raman spectra were obtained using a Renishaw InVIA microspectrometer, equipped with a 532 nm argon laser. The laser was focused on the sample by using a DMLM Leica microscope with a 50×·objective. The spectrometer was first calibrated with a silicon standard before the analytical session. For each target, we determined the Raman shift intensity in the spectral window from 1000 to 1900 cm^{-1} including the first-order disorder carbon (D) and graphite (G) bands. A laser power below 1 mW was used to prevent any thermal alteration during the spectra acquisition. Finally, spectra acquisition was achieved after three successive iterations using a time exposure of 40 seconds.

2.2.3. Nanoscale secondary ion mass spectrometry

Standards and microfossils were analyzed using the CAMECA NanoSIMS 50 at the MNHN. Before measurements, pre-sputtering is required (i) to avoid surficial contamination and (ii) to achieve the saturation fluence of implemented Cesium (Cs^+) in order to obtain constant secondary ion count rates and then, a constant $^{12}C^{14}N^-/^{12}C_2^-$ ionic ratio (Fig. 1). Hence, Cs^+ was implanted using a 200 pA primary current (300 µm aperture diaphragm) on 50×50 to 75×75 $µm^2$ areas, depending of the size of each target. Analyses were then carried out using a 5 pA primary current (150 µm aperture diaphragm) on smaller areas to avoid pre-sputtering edge artifacts. Secondary

molecular ions and species of $^{12}C_2^-$, $^{12}C^{14}N^-$ and $^{28}Si^-$ were collected simultaneously in electron multipliers. NanoSIMS raw data were corrected for a 44 ns dead time on each electron multiplier and were processed using the Limage software (developed by L. Nittler, Carnegie Institution, Washington DC, USA). The external reproducibility was determined through multiple measurements of the emissions of the $^{12}C^{14}N^-$ and $^{12}C_2^-$ molecules on a coal standard used in Thomen et al. (2014). A second NanoSIMS session was dedicated to the analyses of a blank (polycarbonate filter), of pure organic standards (resin and tryptophan) and of a type III kerogen (land plant-derived carbonaceous matter). These pure standards and the type III kerogen correspond to the standards previously used in Alleon et al. (2015). Hence, Cs+ was implanted using a 400 pA primary current (150 µm aperture diaphragm) on 45×45 μm^2 areas. Analyses were then carried out using a 1 pA primary current (150 µm aperture diaphragm) on smaller areas to avoid pre-sputtering edge artifacts.

2.2.4. Statistics and errors

Correlations between the $^{12}C_2^-$ and $^{12}C^{14}N^-$ and $^{28}Si^-$ ion emissions were tested using Spearman's rank correlation. A *p*-value inferior to 0.05 is indicative of a significant correlation. In the presence of a significant spatial relationship between the emissions of ions, linear regressions were performed to calculate the value of the slope and its associated standard error ($1\mathring{u}_{reg}$) following:

$$1\mathring{u}_{reg} = \sqrt{\sum(y_i - \hat{y}_i)^2/(n-2)} \Big/ \sqrt{\sum(x_i - \bar{x})^2} \quad (1)$$

where yi is the emission of the $^{12}C^{14}N^-$ ion measured by NanoSIMS, ŷi is the emission of the $^{12}C^{14}N^-$ ion determined by linear regression, xi is the emission of the $^{12}C_2^-$ ion measured by NanoSIMS, $\bar{x}$ the average value of the emissions of the $^{12}C_2^-$ ion and where n is the number of ROIs.

The external reproducibility was determined by determining the slope of the regression line between the $^{12}C_2^-$ and $^{12}C^{14}N^-$ ion emissions of a coal standard (n = 7). Then, the standard error of the mean slope ñŬô ($1\mathring{u}_{rep}$) was calculated.

Finally, the total error ($1\mathring{u}_{tot}$) was determined as follow:

$$1\square_{\square\square\square} = \square\overline{1\square_{\square\square\square}^{\square} + 1\square_{\square\square\square}^{\square}} \quad (2)$$

3. Results

3.1. Carbonaceous microfossils in thin section and kerogen

A morphological diversity of microfossils was observed in thin section, with assemblages of lenticular (formerly described as spindle-like; *ca.* 20-40 µm; Sugitani et al., 2007; Grey and Sugitani, 2009; Sugitani et al., 2009), film-like (>100 µm), and spheroidal (mainly <15 µm) microfossils occurring either as isolated specimens or as clusters (Fig. 2). In both spheroids and lenticular structures analyzed in thin sections, the $^{12}C_2^-$ and $^{12}C^{14}N^-$ ion emissions (Figs. 2a, b) are found within the siliceous matrix. In the film-like microstructure (Fig. 2c), the $^{12}C_2^-$ and

179 $^{12}C^{14}N^-$ are emitted with almost no emission of $^{28}Si^-$. This observation illustrates the fact that this
180 microstructure was encapsulated by the siliceous matrix.
181 Characterizing microfossils from thin sections using NanoSIMS implies that the analyzed targets
182 occur at the very surface of the sample because the intensity of the primary beam cannot sputter
183 more than a few atomic layers in depth. Therefore, the amount of microfossil targets in thin
184 sections is limited. On the contrary, the kerogen fraction obtained by HF-HCl maceration of the
185 fossil-bearing black cherts contains some microfossils morphologically equivalents to those in
186 thin section (Grey and Sugitani, 2009). Although spheroids identified in the thin section were not
187 found in the kerogen residue, lenticular and film-like microfossils were also observed in the
188 kerogen fraction (Fig. 3). These lenticular and film-like microfossils are characterized by Raman
189 line shape (Fig. 4),which are consistent with previous Raman spectra determined on microfossils
190 from thin section (Sugitani et al., 2007)
191
192 **3.2 NanoSIMS quantitative investigation**
193
194 The N/C atomic ratio has been classically used to assess the preservation status of ancient organic
195 matter (Watanabe et al., 1997; Beaumont and Robert, 1999). Using NanoSIMS analysis, the
196 $^{12}C^{14}N^-/^{12}C_2^-$ ionic ratio has been regarded as a proxy of the N/C atomic ratio for silica-free
197 kerogens or pure organic standards (Thomen et al., 2014; Alleon et al., 2015). However, in case
198 of microfossils, two additional analytical artefacts should be considered (1) matrix effects
199 (chemical heterogeneity) linked to the occurrence of silicate minerals and (2) microtopographic
200 effects yielding a difference in the emissivity of the $^{12}C_2^-$ and $^{12}C^{14}N^-$ ions. Owing to the imaging
201 capability of the NanoSIMS, the $^{12}C_2^-$ and $^{12}C^{14}N^-$ variations have been recorded at a high spatial
202 resolution. In the following, we demonstrate that the spatial variation between $^{12}C_2^-$ and $^{12}C^{14}N^-$ is

linear and that its corresponding slope ñαñ is correlated with the N/C atomic ratio. However, this linear variation between $^{12}C_2^-$ and $^{12}C^{14}N^-$ shows a non-zero intercept ò**β**ò, possibly related to the sample surface microtopography. No relation was found between **β** and α, justifying in turn, the use of α to record the relative variations of the N/C ratio. In addition, no measurable variation in the emissivity of the $^{12}C_2^-$ and $^{12}C^{14}N^-$ ions has been detected in the presence of silicate minerals, avoiding measurable matrix effects on α.

3. 2..1 The slope ñŮò, a record of the N/C atomic ratio

Emissions of $^{12}C_2^-$ and $^{12}C^{14}N^-$ in resin, tryptophan and a type III kerogen are systematically correlated (Figs. 5a and 5b; Table 1). Although both emissions converge towards 0 for lower ion counting rates, the linear regression calculated on the whole range of emissions yields a non-zero intercept ñ**β**ò. This relationship is characterized by a slope ñŮò. In Fig. 5c, the slopes of pure kerogen and standards are reported versus bulk N/C atomic ratio. Note that for a N-free sample (polycarbonate filter) no relationship between the emissions of the $^{12}C_2^-$ and $^{12}C^{14}N^-$ ions is found (Table 1). Hence, a significantly linear relationship between the $^{12}C_2^-$ and $^{12}C^{14}N^-$ ion emissions is the preliminary condition in order to define a slope ñŮò that can be used to record the N/C atomic ratio.

3.2.2.Matrix effect

Oehler et al. (2009) defined a matrix effect in their NanoSIMS measurements as the enhancement of the $^{28}Si^-$ and $^{16}O^-$ ion emissions when these ions are closely and spatially associated with

carbon. Such a matrix effect may be linked to a higher conductibility of Si associated with carbonaceous globules compared to that of Si in the surrounding siliceous minerals. In microfossils from chert thick section (Fig. 6a), no relationship between $^{28}Si^-$ on the one hand and $^{12}C_2^-$ (Fig. 6b) and $^{12}C^{14}N^-$ (Fig. 6c) ion emissions on the other hand has been found. Hence, $\breve{U}$ is not affected by the occurrence of Si.

3.2.3. Microtopography

To investigate the effect of microtopography, we have compared the $^{12}C_2^-$ and $^{12}C^{14}N^-$ ion emissions on two selected flat and non-flat (microtopograhic features between 1 to 10µm) areas from a chemically homogeneous resin standard (Fig. 7a). Fig. 7, it can be seen that microtopography does not cause measurable shift in $\breve{U}$ (Fig. 7b; flat area: $\breve{U}$ = 0.52 ± 0.05; non flat area $\breve{U}$ = 0.56± 0.02).

Fig. 7c shows that the value of the $^{12}C^{14}N^-/^{12}C_2^-$ ratio is not affected by small micrometric scale microtopography up to 2 µm. Although a 10µm of topography can enhance the ionic $^{12}C^{14}N^-/^{12}C_2^-$ ratio by a factor of up to 4, the slope of the correlated variations between $^{12}C^{14}N^-$ and $^{12}C_2^-$ is only related to the N/C atomic ratio of the sample. Such a bias in the determination of the $^{12}C^{14}N^-/^{12}C_2^-$ ratio is also related to the value of the non-zero intercept β, which seems to rise through enhanced microtopography (Figs. 7b and c). In contrast to the $^{12}C^{14}N^-/^{12}C_2^-$ ratio, the slope Ŭ is constant in topographic domain covering 1 to 10 micrometers (Figure 7c). $^{12}C^{14}N^-/^{12}C_2^-$. Note that due to the size of the presently studied microfossils and the fact that microfossil edges were not considered, the microtopographic features cannot exceed a few µm.

248 Consequently, the matrix and microtopograhic effects do not bias the use of the slope ñαò, as a
249 record of the N/C atomic ratio.

250

251 **4. Discussion**

252 Evidence for the permineralization of a part of the microfossils from the Farrel Quartzite
253 was previously suggested by Oehler et al. (2009) owing to the co-emissions of the Si^-, C_2^- and
254 CN^- ions in microfossils from thin section. Here, $^{28}Si^-$ and $^{12}C_2^-$, ions on the one hand and $^{28}Si^-$ and
255 $^{12}C^{14}N^-$ ions on the other hand, were not spatially associated at the pixel scale (Fig. 6). Such
256 findings may echo results observed in the 3.4 Gyr-old Strelley Pool Formation, in which Lepot et
257 al (2013) observed lenticular microfossils composed of carbonaceous globules that were
258 interpreted as degradation by-products of Archean microorganisms. However, in the present
259 study, no 3D carbonaceous globules were observed in the isolated kerogen. Since they did not
260 survive the acid treatment, they must be not considered as encapsulated but rather as
261 permineralized.

262

263 In contrast to carbonaceous globules, carbonaceous microfossils were recovered in the
264 acid maceration residue. Among these microfossils, one example of an exceptional
265 morphological preservation of a lenticular microfossil is shown. Classically, in the literature,
266 lenticular microfossils exhibit two kinds of flange-like appendages situated either in the
267 equatorial plane or at the apical part of the vesicle body (Sugitani et al., 2009; House et al., 2013).
268 Here, the flange-like appendage was situated at the apical part of the vesicle body. Lenticular but
269 also film-like microfossils consist almost entirely of organic matter, suggesting that they are

organic-walled microfossils removed from the silica matrix by the HF treatment. In turn, this result implies the preservation of some organic-walled microfossils by encapsulation rather than by permineralization. These organic-walled microfossils are characterized by equivalent Raman line shape (Fig. 4), corresponding to advanced carbonization/greenschist facies metamorphism in silicified cherts (Delarue et al., 2016). Raman characteristics of the microfossils are then consistent with the thermal history of the Farrel Quartzite cherts (Sugitani et al., 2007) revealing, in turn, their syngenecity.

The slope ñŬò parameter for both permineralized and encapsulated microfossils was calculated as a proxy of the *in situ* N/C atomic ratio (Fig. 8; Table 2). The correlation between $^{12}C_2^-$ and $^{12}C^{14}N^-$ is statistically significant for eleven out of the fourteen analyzed microfossils (Table 2), which will be considered in the following discussion.

In the permineralized lenticular and spheroid microfossils, ***Ŭ*** ranges from 0.03 to 0.19 whereas it ranges from 0.05 to 1.84 in the encapsulated lenticular and film-like ones (Table 2). First of all, these data suggest that there is an unexpected geochemical heterogeneity among the microfossils preserved in the 3.0 Gyr-old Farrel Quartzite. Most of the encapsulated microfossils are characterized by a greater Ŭcompared to permineralized ones (Fig. 8; Table 2). This indicates that encapsulated microfossils present higher geochemical preservation level than the permineralized ones, and that the mode of fossilization may a key controlling factor in the geochemical heterogeneity in the Farrel Quartzite carbonaceous matter. Finally, this difference in the extent of geochemical preservation between permineralized and encapsulated microfossils is consistent with observations made on modern microbial mat that show that microorganisms are better preserved through encapsulation (Konhauser and Ferris, 1996). Focusing future studies on

293 Archean encapsulated microfossils may then provide the best geochemical evidence in the search
294 for traces of terrestrial early-life.
295

296 **Conclusion**

297 In this study, we provide new lines of evidence supporting the partial fossilization of
298 carbonaceous microfossils through encapsulation in the *ca*. 3.0 billion-years-old cherts from the
299 Farrel Quarzite in the Pilbara craton, Western Australia. Encapsulated microfossils were observed
300 both in the thin section and in the kerogen fraction. Using the slope ñŭo parameter relating the
301 $^{12}C_2^-$ and $^{12}C^{14}N^-$ NanoSIMS emissions as an index of geochemical preservation of the studied
302 microfossils, we demonstrate that encapsulated microfossils present higher level of geochemical
303 preservation than permineralized ones. Thus, the mechanism of fossilization of microorganisms
304 may be considered as a key controlling factor in preserving geochemical heterogeneity.
305 Overall our results suggest that focusing *in situ* investigations on well preserved encapsulated
306 carbonaceous matter may provide the best chance to recover information on the earliest forms of
307 terrestrial life that are likely to be lost in bulk investigations.
308

309 **Acknowledgements**

310 The authors are thankful to J.J. Pantel for his help in sample crushing. The authors are also
311 grateful to A. Gonzalez-Cano and S. Mostefaoui for elemental measurements at the National
312 NanoSIMS Facility of the MNHN, to S. Bernard for providing NanoSIMS standards, to S. Pont
313 for microfossil imaging at the SEM Facility of the MNHN and to O. Belhadj (Center for
314 Research on the Preservation of Collections, USR 3224). This work was supported by the ERC

315 project ñPaleoNanoLifeò and by the Japanese Society for the Promotion of Science (a grant-in-
316 aid No. 24654162). Special thanks to Tsutomu Nagaoka (Nagoya University) for assistance in
317 preparation of thin section and to Dr. K. Grey (Western Australia) for permission for sample
318 export.

319

320 **Disclosure statement**

321 No competing financial interests exist.

322

323 **References**

324 Alleon, J., Bernard, S., Remusat, L. and Robert, F. (2015) Estimation of nitrogen-to-carbon ratios
325 of organics and carbon materials at the submicrometer scale. *Carbon* 84: 290-298.
326 Alleon, J., Bernard, S., Le Guillou, C., Marin-Carbonne, J., Pont, S., Beyssac, O., McKeegan,
327 K.D. and Robert, F. (2016) Molecular preservation of 1.88 Ga Gunflint organic microfossils as a
328 function of temperature and mineralogy. *Nature Communications* 7: doi: 10.1038/ncomms11977
329 Beaumont, V. and Robert, F. (1999) Nitrogen isotope ratios of kerogens in Precambrian cherts: a
330 record of the evolution of atmosphere chemistry? *Precambrian Research* 96: 63-82.
331 Delarue, F., Rouzaud, J-N., Derenne, S., Bourbin, M., Westall, F., Kremer, B., Sugitani, S.,
332 Deldicque, D. and Robert, F. (2016) The Raman-Derived Carbonization Continuum:A Tool to
333 Select the Best Preserved Molecular Structures in Archean Kerogens. *Astrobiology* 16 (6): 407ï
334 417.
335 Derenne, S., Robert, F., Skrzypczak-Bonduelle, A., Gourier, D., Binet, L. and Rouzaud, J.-N.

(2008) Molecular evidence for life in the 3.5 billion year old Warrawoona chert. *Earth and Planetary Science Letters* 272: 476-480.

Grey, K. and Sugitani, K. (2009) Palynology of Archean microfossils (c. 3.0 Ga) from the Mount Grant area, Pilbara Craton, Western Australia: Further evidence of biogenicity. *Precambrian Research* 173: 60-69.

House, C. H., Oehler, D. Z., Sugitani, K. and Mimura, K. (2013) Carbon isotopic analyses of ca. 3.0 Ga microstructures imply planktonic autotrophs inhabited Earth's early oceans. *Geology* 41 (6): 651-654.

Javaux, E.J., Marshall, C.P. and Bekker, A. (2010) Organic-walled microfossils in 3.2-billion-year-old shallow-marine siliciclastic deposits. *Nature* 463, 934-U108.

Konhauser, K.O. and Ferris, F.G. (1996) Diversity of iron and silica precipitation by microbial mats hydrothermal waters, Iceland: Implications for Precambrian iron formations. *Geology* 24: 323-326.

Lepot, K., Williford, K.H., Ushikubo, T., Sugitani, K., Mimura, K., Spicuzza, M.J., Valley, J.W. (2013) Texture-specific isotopic compositions in 3.4 Gyr old organic matter support selective preservation in cell-like structures. *Geochimica Et Cosmochimica Acta* 112: 66-86.Oehler, D.Z., Robert, F., Walter, M.R., Sugitani, K., Allwood, A., Meibom, A., Mostefaoui, S., Selo, M., Thomen, A. and Gibson, E.K. (2009) NanoSIMS: Insights to biogenicity and syngeneity of Archaean carbonaceous structures. *Precambrian Research* 173: 70-78.

Oehler, DZ., Robert, F., Walter, MR., Sugitani, K., Meibom, A., Mostefaoui, S. and Gibson, EK. (2010) Diversity in the Archean biosphere: new insights from NanoSIMS. *Astrobiology* 10: 413ï 424.

358 Picard, A., Kappler, A., Schmid, G., Quaroni, L. and Obst, M. (2015) Experimental diagenesis of
359 organo-mineral structures formed by microaerophilic Fe(II)-oxidizing bacteria. *Nature*
360 *Communications* 6: doi: 10.1038/ncomms7277

361 Rainey, D.K. and Jones, B. (2010) Preferential soft-tissue preservation in the Hot Creek
362 carbonate spring deposit, British Columbia, Canada. *Sedimentary Geology* 227: 20-36.

363 Schopf, J.M. (1975) Modes of fossil preservation. Review of Palaeobotany and *Palynology* 20:
364 27-53.

365 Schopf, J.W. (1993) Microfossils of the early Archean apex chert - new evidence of the antiquity
366 of life. *Science* 260: 640-646.

367 Sugitani, K., Grey, K., Allwood, A., Nagaoka, T., Mimura, K., Minami, M., Marshall, C.P., Van
368 Kranendonk, M.J. and Walter, M.R. (2007) Diverse microstructures from Archaean chert from the
369 mount goldsworthy-mount grant area, pilbara craton, western australia: Microfossils,
370 dubiofossils, or pseudofossils? *Precambrian Research* 158: 228-262.

371 Sugitani, K., Grey, K., Nagaoka, T. and Mimura, K. (2009) Three-Dimensional Morphological
372 and Textural Complexity of Archean Putative Microfossils from the Northeastern Pilbara Craton:
373 Indications of Biogenicity of Large (> 15 μm) Spheroidal and Spindle-Like Structures.
374 *Astrobiology* 9: 603-615.

375 Sugitani, K., Lepot, K., Nagaoka, T., Mimura, K., Van Kranendonk, M., Oehler, D.Z. and Walter,
376 M.R. (2010) Biogenicity of Morphologically Diverse Carbonaceous Microstructures from the ca.
377 3400Ma Strelley Pool Formation, in the Pilbara Craton, Western Australia. *Astrobiology* 10: 899-
378 920.

379 Sugitani, K., Mimura, K., Lepot, K., Takeuchi, M., Ito, S. and Javaux, E.J. (2015) Early evolution
380 of large microorganisms with cytological complexity revealed by microanalyses of 3.4 Ga
381 organic-walled microfossils. *Geobiology* 13(6): 507ï 521.
382 Thomen, A., Robert, F. and Remusat, L. (2014) Determination of the nitrogen abundance in
383 organic materials by NanoSIMS quantitative imaging. *Journal of Analytical Atomic Spectrometry*
384 29: 512-519.
385 Walsh, M.M. (1992) Microfossils and possible microfossils from the early archean Onverwacht
386 group, Barberton mountain land, South-Africa. *Precambrian Research* 54: 271-293.
387 Watanabe, K., Naraoka, H., Wronkiewicz, DJ., Condie, KC., Ohmoto, H. (1997) Carbon,
388 nitrogen, and sulfur geochemistry of Archean and Proterozoic shales from the Kaapvaal Craton,
389 South Africa. *Geochimica Et Cosmochimica Acta* 61: 3441-3459.
390

Figure captions

FIG.1. $^{12}C^{14}N^{-}/^{12}C_2^{-}$ ratio recorded as a function of the presputterring duration. The grey area indicates the time window in which the saturation fluence was achieved on the resin standard. Saturation fluence was systematically controlled for each studied microfossils.

FIG.2. Transmitted light photomicrographs and NanoSIMS ion images ($^{12}C_2^{-}$, $^{12}C^{14}N^{-}$ and $^{28}Si^{-}$) of (**a**) a lenticular-like microfossil, (**b**) a spheroid cluster, and (**c**) a film-like microfossil. The microfossils were all observed on thin section. On each photomicrograph, the red dashed square outline indicates the area investigated by NanoSIMS.

FIG.3. (a) Secondary electron and X-ray images of selected elements for a film-like and a well-preserved lenticular-like isolated microfossils. **(b)** NanoSIMS ion images ($^{12}C_2^{-}$, $^{12}C^{14}N^{-}$ and $^{28}Si^{-}$) determined on the filament-like microfossil and on the two distinct ultrastructures of the well-preserved lenticular-like microfossil, namely the vesicle body and the flange-like appendage.

FIG.4. First-order Raman spectrum of the filaments and the lenticular microfossils presented in Fig. 3.

FIG.5. (a) NanoSIMS ion images ($^{12}C_2^-$ and $^{12}C^{14}N^-$) of type III kerogen, resin and tryptophan. (b) Relationship between the emissions of $^{12}C_2^-$ and $^{12}C^{14}N^-$ ions in each standard. Each point is related to a ROI (n=30) manually drawn on the flattest part of the standards following the procedure described in Alleon et al. (2015; see Table 1 for further information about the number and size of ROIs). (c) Determination of the N/C atomic ratio by the use of the $^{12}C^{14}N^-/^{12}C_2^-$ ionic ratio (Thomen et al., 2014; Alleon et al., 2015) and the slope "***Ŭ***". Note that coal and microfossils (session 1) were not studied in the same analytical session than the 3 standards (session 2) used to calibrate the use of the slope α as a proxy of the N/C atomic ratio. Accordingly, this prevents any calculation of in situ N/C atomic ratios of microfossils.. Also, note the linear relationship in each case, which evidences the absence of matrix effect on the determination of both $^{12}C^{14}N^-/^{12}C_2^-$ ionic ratio and the slope "α".

FIG.6. (a) NanoSIMS images ($^{12}C_2^-$) of microfossils from thin section (presented in Fig. 2) displaying the ROIs used to study the potential relationship between (b) the $^{28}Si^-$ and the $^{12}C_2^-$ ions and (c) the $^{28}Si^-$ and the $^{12}C^4N^-$ ions. In order to constrain the spatial variability of the emissions of the $^{12}C_2^-$ and $^{12}C^{14}N^-$ ions,

ROIs were manually drawn around carbon/silica in permineralized microfossils. For encapsulated microfossils, a grid was used (see Table 1 for further information on the number and the size of the ROIs).

FIG.7. Investigation of the effect of microtopography on the determination of the slope "***Ŭ***" and its error on a (a) $^{12}C_2^-$ and $^{12}C^{14}N^-$ ion flat (left images) and non-flat (right images) areas from the resin standards. In the non-flat area, photonic microtopography was created through extensive sputtering (1, 2 and 12 hours) leading to the creation of micrometric scale microtopography estimated through microscopy (ca. 1, 2 and 10 µm depth, respectively). The relationship between the emissions of $^{12}C_2^-$ and $^{12}C^{14}N^-$ ions was estimated (i) on the above (i) flat area using 30 ROIs (yellow circles of 0.8 µm diameter) as suggested by Alleon et al. (2015) and (ii) non-flat area using 121 ROIs (red grid, each square has a width of 2.2 µm). (b) Relationships between the emissions of $^{12}C_2^-$ and $^{12}C^{14}N^-$ ions in the flat and the non-flat areas. (c) Comparison between the $^{12}C^{14}N^-/^{12}C_2^-$ ionic ratio calculated as in Alleon et al. (2015) and the slope "***Ŭ***" (this study) values across microscale microtopography. The red area indicates the values of the slope "***Ŭ***" determined on the flat area. The intercept of the linear regression between the emissions of $^{12}C_2^-$ and $^{12}C^{14}N^-$ ions is noted "β".

FIG.8. (a) Relationships between the emissions of $^{12}C_2^-$ and $^{12}C^{14}N^-$ ions in microfossils from thin section (b) Relationship between the emissions of $^{12}C_2^-$ and $^{12}C^{14}N^-$ ions in encapsulated microfossils from the kerogen residue.

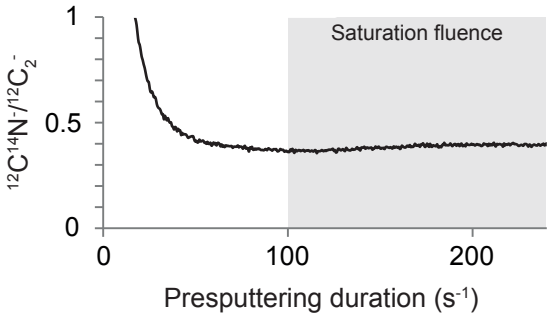
Saturation fluence
1
0.5
0
0
100
200
$^{12}C^{14}N^-/^{12}C_2^-$
Presputtering duration (s^{-1})

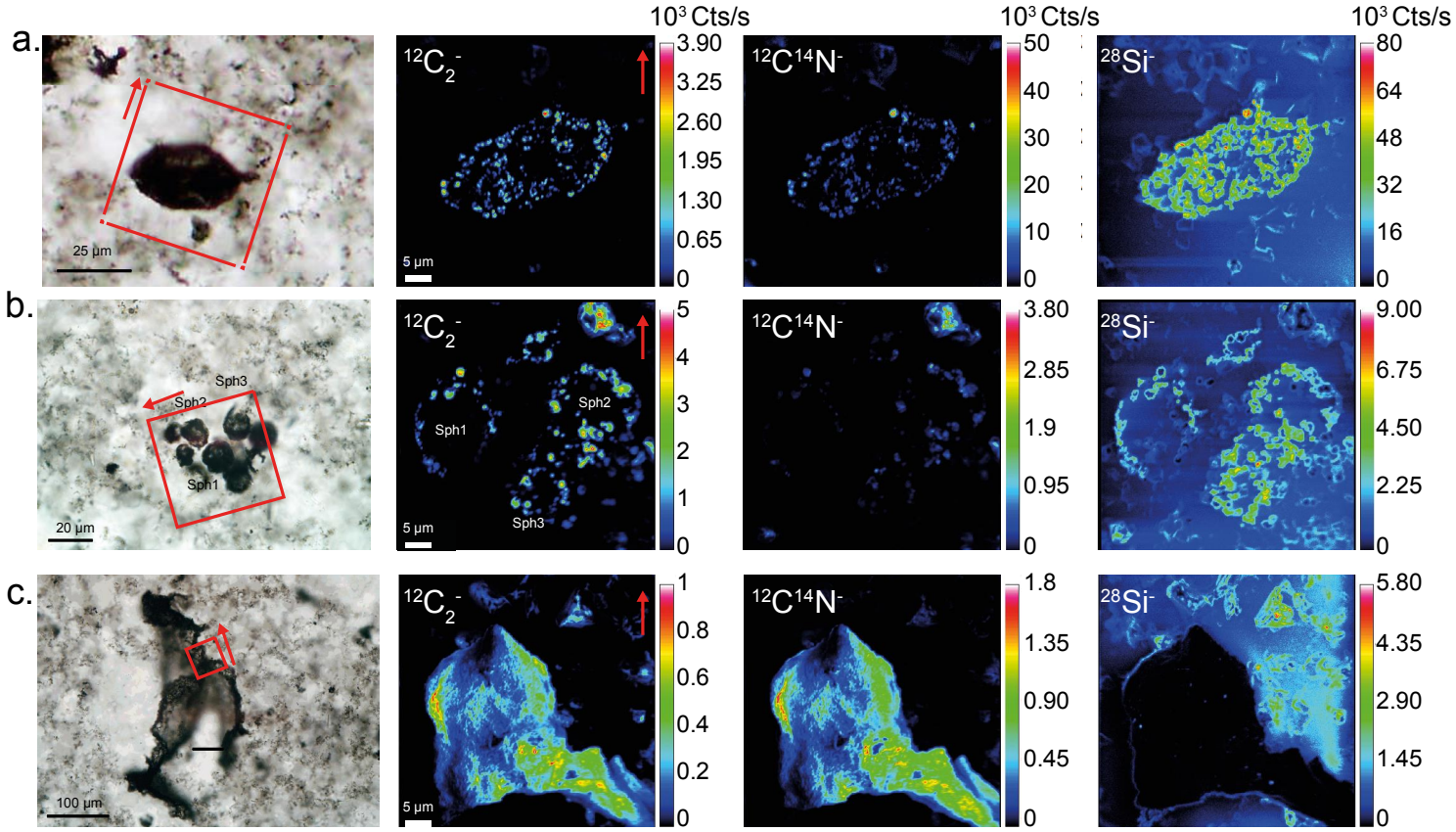
a.
b.
c.
25 µm
20 µm
100 µm
Sph1
Sph2
Sph3
$^{12}C_2^-$
$^{12}C^{14}N^-$
$^{28}Si^-$
10^3 Cts/s
5 µm
3.90
3.25
2.60
1.95
1.30
0.65
0
50
40
30
20
10
80
64
48
32
16
5
4
3
2
1
3.80
2.85
1.9
0.95
9.00
6.75
4.50
2.25
1
0.8
0.6
0.4
0.2
1.8
1.35
0.90
0.45
5.80
4.35
2.90
1.45

a.

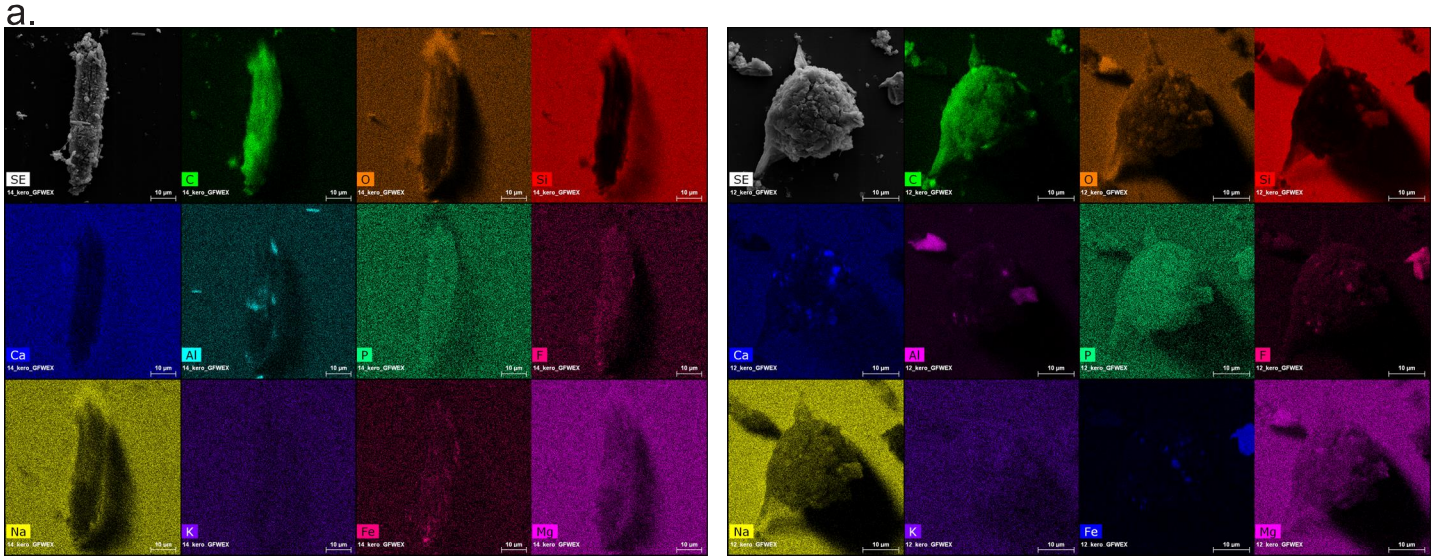
SE
C
O
Si
Ca
Al
P
F
Na
K
Fe
Mg

b.

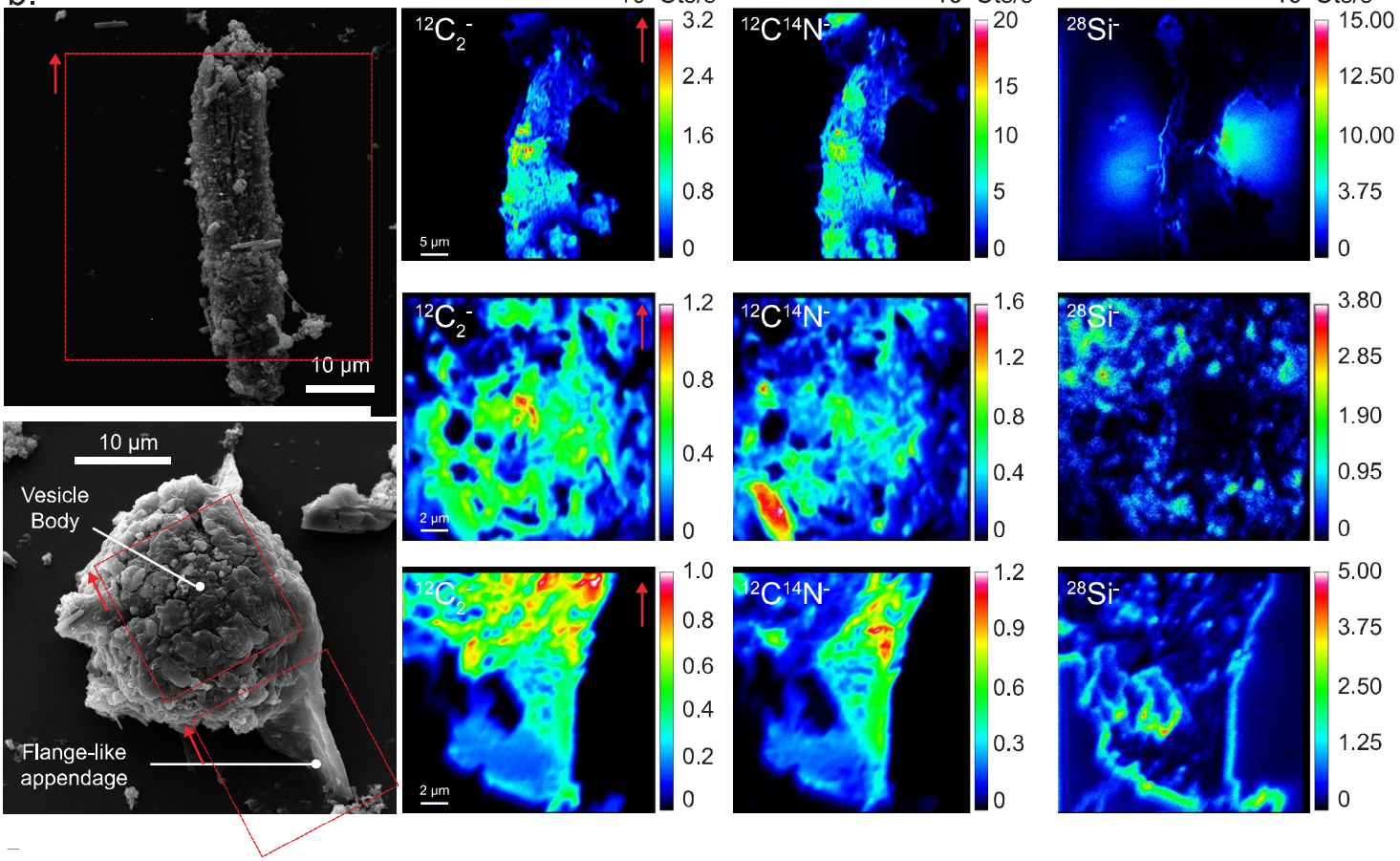
10 µm
Vesicle Body
Flange-like appendage
$^{12}C_2^-$
$^{12}C^{14}N^-$
$^{28}Si^-$
10^3 Cts/s
5 µm
2 µm
3.2
2.4
1.6
0.8
0
20
15
10
5
15.00
12.50
10.00
3.75
1.2
0.4
1.6
3.80
2.85
1.90
0.95
1.0
0.6
0.2
1.2
0.9
0.3
5.00
2.50
1.25

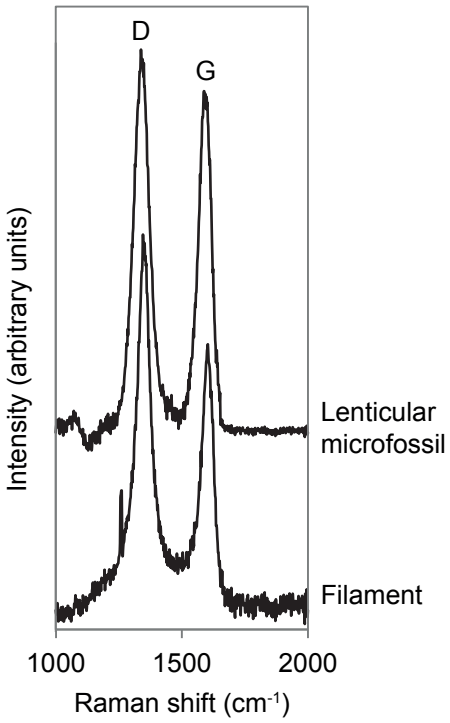
D
G
Intensity (arbitrary units)
Lenticular microfossil
Filament
1000
1500
2000
Raman shift (cm-1)

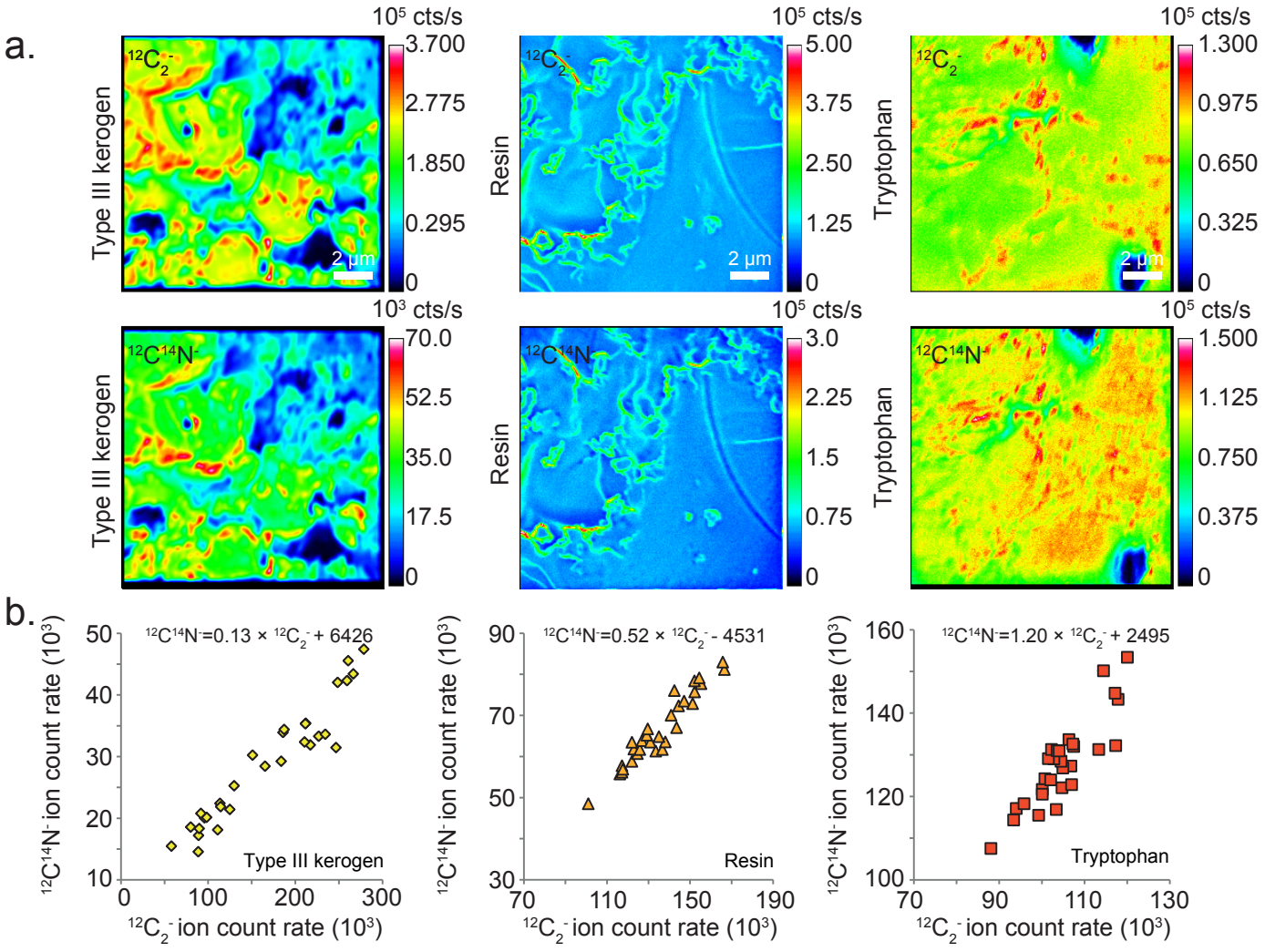
a.
Type III kerogen
Resin
Tryptophan
$^{12}C_2^-$
$^{12}C^{14}N^-$
10^5 cts/s
10^3 cts/s
2 µm
b.
$^{12}C^{14}N^-$=0.13 × $^{12}C_2^-$ + 6426
$^{12}C^{14}N^-$=0.52 × $^{12}C_2^-$ - 4531
$^{12}C^{14}N^-$=1.20 × $^{12}C_2^-$ + 2495
$^{12}C^{14}N^-$ ion count rate (10^3)
$^{12}C_2^-$ ion count rate (10^3)
c.
$^{12}C^{14}N^-/^{12}C_2^-$ ionic ratio and α
Bulk N/C atomic ratio
$^{12}C^{14}N^-/^{12}C_2^-$ (Thomen et al., 2014)
$^{12}C^{14}N^-/^{12}C_2^-$ (Alleon et al., 2015)
α (this study)
Type III kerogen
Resin
Tryptophan

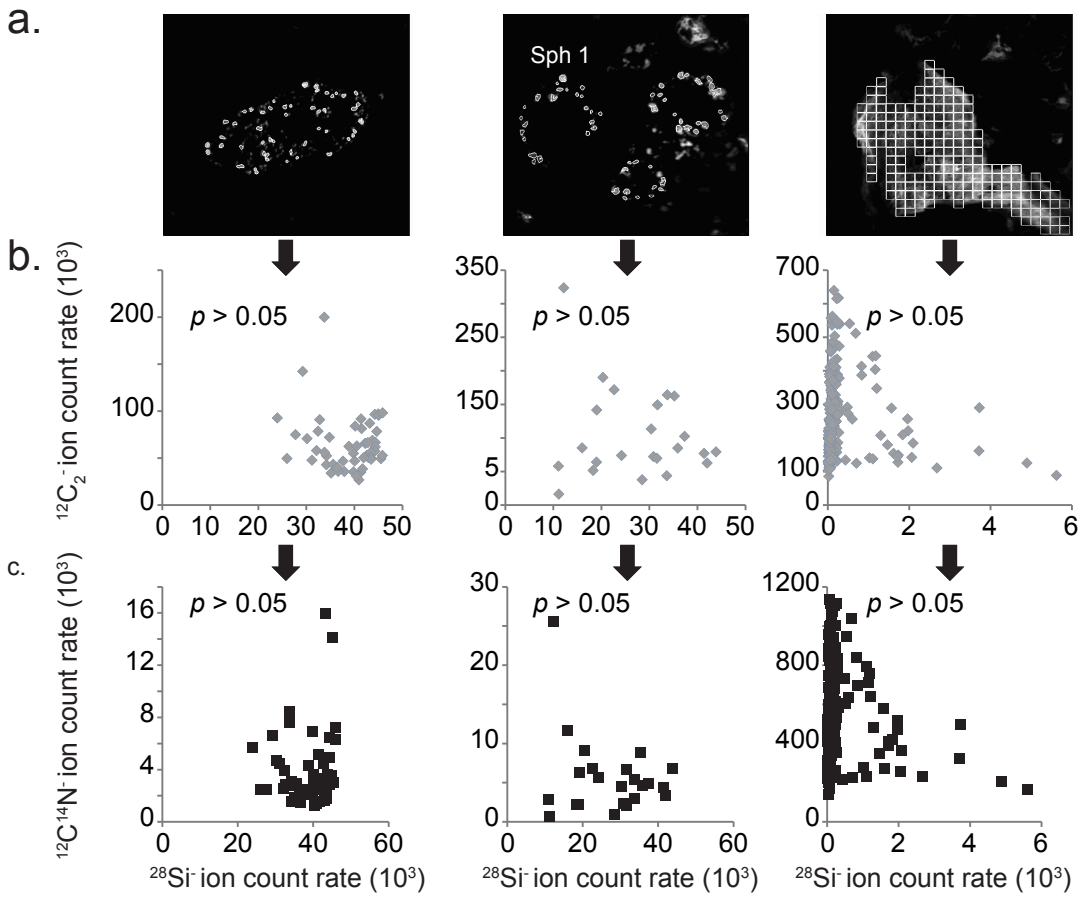
a.
Sph 1
b.
c.
$^{12}C_2^-$ ion count rate (10^3)
$^{12}C^{14}N^-$ ion count rate (10^3)
$^{28}Si^-$ ion count rate (10^3)
$^{28}Si^-$ ion count rate (10^3)
$^{28}Si^-$ ion count rate (10^3)
$p > 0.05$
$p > 0.05$
$p > 0.05$
$p > 0.05$
$p > 0.05$
$p > 0.05$
0 10 20 30 40 50
0 10 20 30 40 50
0 2 4 6
0 20 40 60
0 20 40 60
0 2 4 6

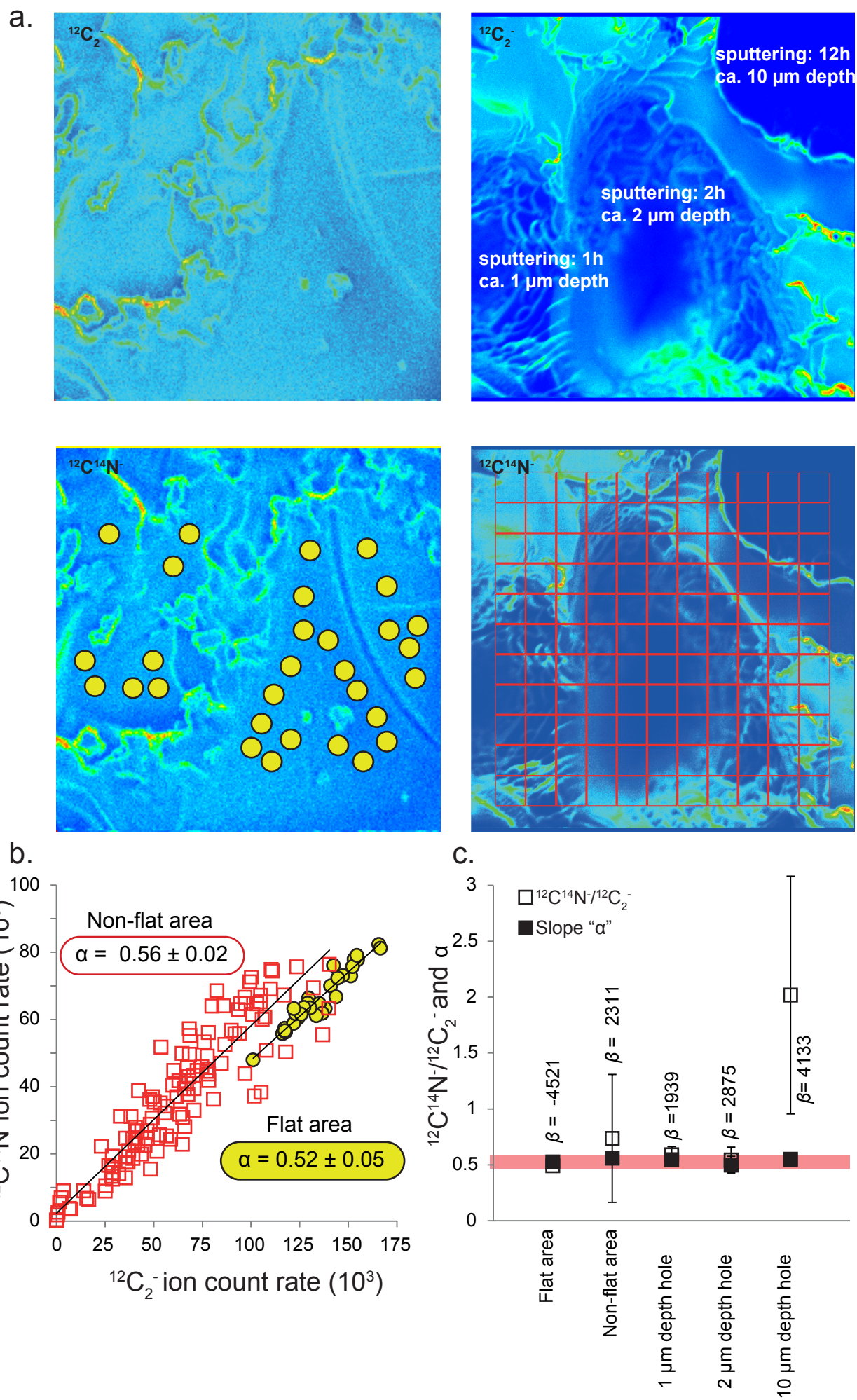
a.
$^{12}C_2^-$
$^{12}C_2^-$
sputtering: 12h
ca. 10 µm depth
sputtering: 2h
ca. 2 µm depth
sputtering: 1h
ca. 1 µm depth
$^{12}C^{14}N^-$
$^{12}C^{14}N^-$
b.
Non-flat area
α = 0.56 ± 0.02
Flat area
α = 0.52 ± 0.05
$^{12}C^{14}N^-$ ion count rate (10^3)
$^{12}C_2^-$ ion count rate (10^3)
0
20
40
60
80
100
0
25
50
75
100
125
150
175
c.
$^{12}C^{14}N^-/^{12}C_2^-$
Slope "α"
$^{12}C^{14}N^-/^{12}C_2^-$ and α
β = -4521
β = 2311
β =1939
β = 2875
β= 4133
0
0.5
1
1.5
2
2.5
3
Flat area
Non-flat area
1 µm depth hole
2 µm depth hole
10 µm depth hole

Fig. 2a: Lenticular microfossil

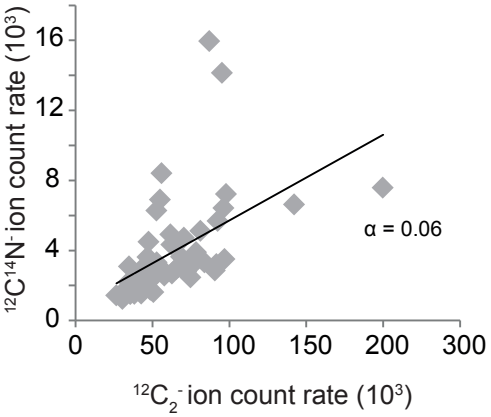

Fig. 2b: Spheroid n°1

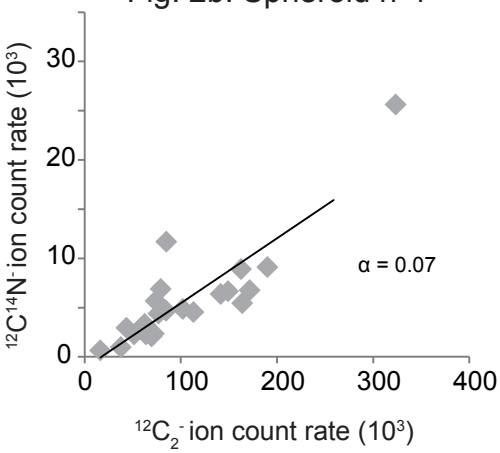

Fig. 2c: Film

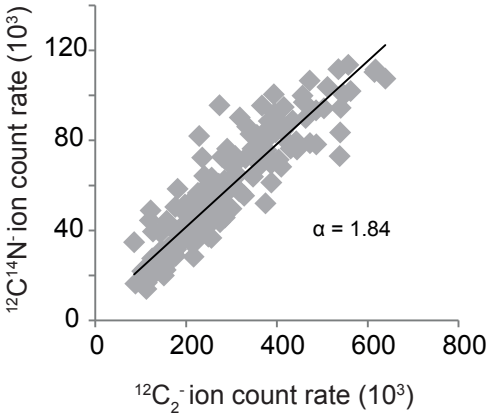

Fig. 3: Filament

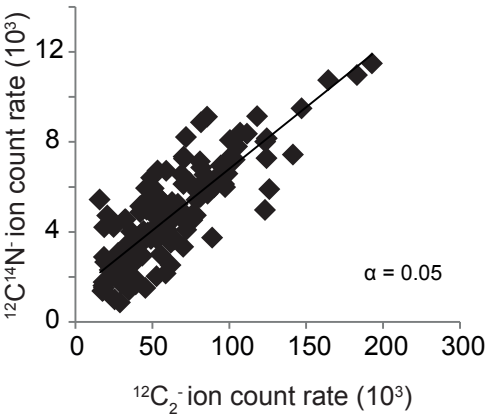

Fig. 3: Vesicle Body

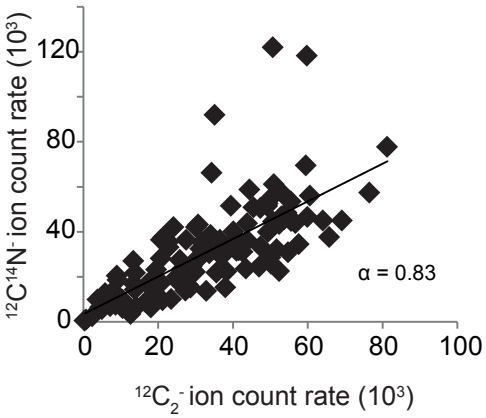

Fig. 3: Flange

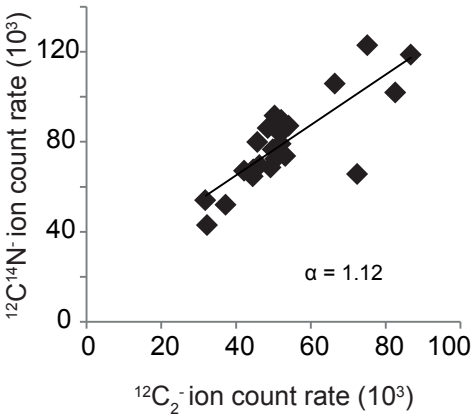

Table 1. Bulk N/C atomic ratio (Thomen et al., 2014; Alleon et al., 2015) of studied standards, number and size of regions of interest (ROIs) used (i) to test the correlation between the emissions of the $^{12}C_2^-$ and $^{12}C^{14}N^-$ ions by using Spearman's rank correlation and (ii) to determine the slope ñŬõ on standards. To minimize the effect of microtopography, ROIs were selected in the flattest part of the standard as recommended by Alleon et al. (2015). In the specific case of the coal standard, our purpose was to measure the external reproducibility. Thus, a maximum of ROIs were selected to characterize the strict effect of analytical drift avoiding then to take into account twice the effect of microtopography during the analyses of microfossils Note that the polycarbonate filter was used as a nitrogen blank in which the $^{12}C_2^-$ and $^{12}C^{14}N^-$ ion emissions are not significantly correlated

Purpose	**Sample**	**Bulk N/C atomic ratio**	**number of ROIs**	**ROIs diameter (µm)**	**Spearman *p*-value**	**Ŭ ± 1ů$_{reg}$**
Blank	Polycarbonate Filter	-	30	1.5	0.50	-
Calibration line	Type III kerogen	0.016	30	1.5	< 0.0001	0.13 ± 0.01
	Resin	0.053	30	0.8	< 0.0001	0.52 ± 0.05
	Tryptophan	0.182	30	1.5	< 0.0001	1.20 ± 0.13
External reproduciblity	Coal 1	0.0022	545	1.1	< 0.0001	0.11 ± 0.004
	Coal 2	0.0022	460	1.1	< 0.0001	0.10 ± 0.002
	Coal 3	0.0022	457	1.3	< 0.0001	0.09 ± 0.002
	Coal 4	0.0022	478	1.3	< 0.0001	0.09 ± 0.004
	Coal 5	0.0022	321	1.3	< 0.0001	0.13 ± 0.003
	Coal 6	0.0022	365	1.3	< 0.0001	0.09 ± 0.002
	Coal 7	0.0022	367	1.4	< 0.0001	0.08 ± 0.004

Table 2. Number and diameter of ROIs used on studied microfossils (microfossils presented in Figs; 2, 3 and 8 are indicated by the superscript a,b and c, respectively). Spearman's rank correlation, slope ñŬòand associated error ($1\mathring{u}_{tot}$) determined through the linear relationship between the emissions of the $^{12}C_2^-$ and $^{12}C^{14}N^-$ ions in both permineralized and encapsulated microfossils from thin section and kerogen.

Microfossil type	Thin section (TS) vs Kerogen (K)	Encapsulated (E) vs Permineralized (P)	number of ROIs	ROI diameter (µm ± SD)	Spearman *p*-value	Ŭ± $1\mathring{u}_{tot}$
Lenticular	TS	P	25	0.63 ± 0.15	0.0013	0.19 ± 0.05
Lenticular[a,c]	TS	P	49	0.66 ± 0.12	< 0.0001	0.06 ± 0.01
Lenticular	TS	P	42	0.78 ± 0.20	0.0002	0.07 ± 0.02
Spheroid	TS	P	52	0.66 ± 0.11	< 0.0001	0.03 ± 0.01
Spheroid	TS	P	25	0.65 ± 0.40	0.14	-
Spheroid 1 [a,c]	TS	P	23	0.94 ± 0.27	< 0.0001	0.07 ± 0.01
Spheroid 2	TS	P	20	1.08 ± 0.52	0.01	0.11 ± 0.05
Spheroid 3	TS	P	13	0.70 ± 0.38	0.11	-
Film	TS	E	252	2.9	< 0.0001	1.48 ± 0.13
Filament[b,c]	K	E	146	2.4	< 0.0001	0.05 ± 0.00
Film	K	E	45	1.3	0.11	-
Film[a,c]	TS	E	195	2.2	< 0.0001	1.84 ± 0.14
Lenticular (vesicle)[b,c]	K	E	121	1.2	< 0.0001	0.83 ± 0.09
Lenticular (flange)[b,c]	K	E	28	0.7	< 0.0001	1.12 ± 0.18